QUANTUM OPTICS

Momentum-exchange interactions in a Bragg atom interferometer suppress Doppler dephasing

Chengyi Luo, Haoqing Zhang, Vanessa P. W. Koh, John D. Wilson, Anjun Chu, Murray J. Holland, Ana Maria Rey, James K. Thompson*

Large ensembles of laser-cooled atoms interacting through infinite-range photon-mediated interactions are powerful platforms for quantum simulation and sensing. Here we realize momentum-exchange interactions in which pairs of atoms exchange their momentum states by collective emission and absorption of photons from a common cavity mode, a process equivalent to a spin-exchange or XX collective Heisenberg interaction. The momentum-exchange interaction leads to an observed all-to-all Ising-like interaction in a matter-wave interferometer. A many-body energy gap also emerges, effectively binding interferometer matter-wave packets together to suppress Doppler dephasing in analogy to Mössbauer spectroscopy. The tunable momentum-exchange interaction expands the capabilities of quantum interaction–enhanced matter-wave interferometry and may enable the realization of exotic behaviors, including simulations of superconductors and dynamical gauge fields.

Many-body quantum states of laser-cooled atoms can be exquisitely controlled, making them powerful platforms for quantum simulation, metrology, and computing. In particular, quantum sensing and metrology rely on understanding how to engineer interatomic interactions to improve the precision of quantum sensors and to emulate both complex quantum phases of matter and nonequilibrium systems that are difficult to access in real materials.

Optical cavities can be used to enhance the interaction of atoms with light in quantum many-body systems in which either the atomic internal (*1*–*5*), motional (*6*–*10*), or both (*11*, *12*) degrees of freedom are coupled between different atoms. In addition, the strong light-atom interaction has enabled large entanglement generation (*13*, *14*), with applications in quantum sensing with matter-wave interferometers (*12*) and clocks (*14*–*17*).

Here, we realize a unitary cavity-mediated momentum-exchange interaction in a many-body system in which pairs of atoms exchange their momentum states (Fig. 1, A and B). The momentum-exchange interaction arises from an atomic density grating creating sideband tones on an applied dressing laser, similar to what occurs in cavity optomechanical systems (*18*–*26*) (Fig. 1, C to E). The momentum exchange can be modeled as an all-to-all pseudospin-exchange interaction, analogous to that observed for internal spin states (*2*–*5*, *27*). Whereas previous theoretical proposals have considered the generation of such momentum exchange in a ring cavity, as well as extensions to two-mode squeezing involving additional spin degrees of freedom (*28*, *29*), here we experimentally realize a momentum-exchange interaction in a standing-wave cavity by exploiting the Doppler shift of the falling atoms.

The observed momentum-exchange interaction allows for the realization of the collective XX-Heisenberg model, an iconic model in quantum magnetism and superconductivity (*30*–*32*), in a momentum-only basis of states with no internal atomic degrees of freedom involved, as compared to previous (*2*–*4*, *27*) and contemporaneous work (*33*). The exchange interaction manifests first as a magnetization-dependent global spin precession of the collective pseudospin Bloch vector, referred to as one-axis twisting (OAT). Second, it generates a many-body energy gap that realizes a collective recoil mechanism that suppresses dephasing owing to Doppler broadening (i.e., single-particle dispersion); this mechanism is analogous to, but distinct from, that employed in Mössbauer and Lamb-Dicke spectroscopy (*34*, *35*).

Experimental setup

In the experiment, ^{87}Rb atoms are laser-cooled inside a two-mirror standing-wave cavity that is vertically oriented along $\hat{Z}$ (Fig. 1A) (*12*, *36*). The atoms are allowed to fall along the cavity axis, guided by a blue detuned intracavity optical dipole trap. A pair of laser beams with different frequencies are injected nonresonantly into the cavity to drive velocity-sensitive two-photon Raman transitions between ground hyperfine states (for state preparation and readout) or Bragg transitions that only change momentum states (for manipulating the superposition of momentum states).

The atoms are prepared in the ground hyperfine state $|F = 2, m_F = 2\rangle$ with momentum along the cavity axis $p_0 - \hbar k$ and root mean square (RMS) momentum spread $\sigma_p < 0.1\hbar k$ after Raman velocity selection from the laser-cooled cloud (*12*), where $\hbar$ is the reduced Planck constant, the wave number is $k = 2$ and the wavelength is $\lambda = 780$ nm. As shown in Fig. 1C, the Bragg lasers are then applied to place the atoms in a superposition of two wave packets with momenta centered on $p_0 \pm \hbar k$ and separated by two-photon recoil momenta $2\hbar k$. The average momentum p_0 continues to increase owing to gravity, but we compensate this by appropriate chirping of applied laser frequencies (*12*, *37*), such that one can consider p_0 to be constant in the following discussion for simplicity. Inserting additional Bragg pulses, we can realize a matter-wave interferometer, in which the atomic wave packets move apart and then reoverlap at a later time. Just after the wave packet splitting and just before reoverlapping, the two portions of the wave packets interfere, leading to a spatially varying atomic density grating with periodicity $\lambda/2$ matching the periodicity of the standing-wave cavity mode.

As shown in Fig. 1E, a cavity mode's frequency is detuned by about 500 MHz to the blue of the D2 cycling transition $|F = 2, m_F = 2\rangle \rightarrow |F' = 3, m_F = 3\rangle$. A dressing laser with photon flux $|\alpha_d|^2$ (in units of photons per second) drives the cavity at frequency ω_d that is typically within a megahertz of the cavity resonance frequency. The input coupling of the cavity κ_1 is determined by the transmission of the input mirror. The detuning of the dressing laser from the atomic transition, Δ_a, is large compared to all other relevant frequency scales, including the excited-state decay rate $\Gamma = 2\pi \times 6$ MHz and the cavity power decay rate $\kappa = 2\pi \times 56(3)$ kHz. In this far-detuned limit, an atom at position Z shifts the cavity resonance by $\frac{g_0^2}{\Delta_a}\cos^2(kZ)$, where $g_0 = 2\pi \times 0.48$ MHz is the maximal Jaynes-Cummings atom-cavity coupling at a cavity antinode (*38*).

Modulation sidebands

As the atomic density grating moves along the cavity axis at velocity $v_0 = p_0/m$, with m the mass of ^{87}Rb, the density grating goes from being aligned to misaligned with the cavity standing wave (Fig. 1D, from left to right). This leads to a modulation of the cavity resonance frequency at the two-photon Doppler frequency $\omega_z = 2kv_0$ (Fig. 1E). The modulation of the cavity resonance frequency leads to optical modulation sidebands on the dressing laser inside the cavity at frequencies $\omega_d \pm \omega_z$, with the closer-to-resonance sideband shown in Fig. 1E (black wiggly line), in a direct analogy to cavity optomechanical systems (*24*–*26*). The modulation sidebands can also be understood as the Doppler-shifted reflection of the dressing laser from the moving matter-wave grating.

We directly observe that a modulation sideband, combined with the dressing laser, form a Bragg coupling that drives collective population transfer from $p_0 - \hbar k$ to $p_0 + \hbar k$ as

JILA, NIST, and Department of Physics, University of Colorado, Boulder, CO, USA.
*Corresponding author. Email: jkt@jila.colorado.edu

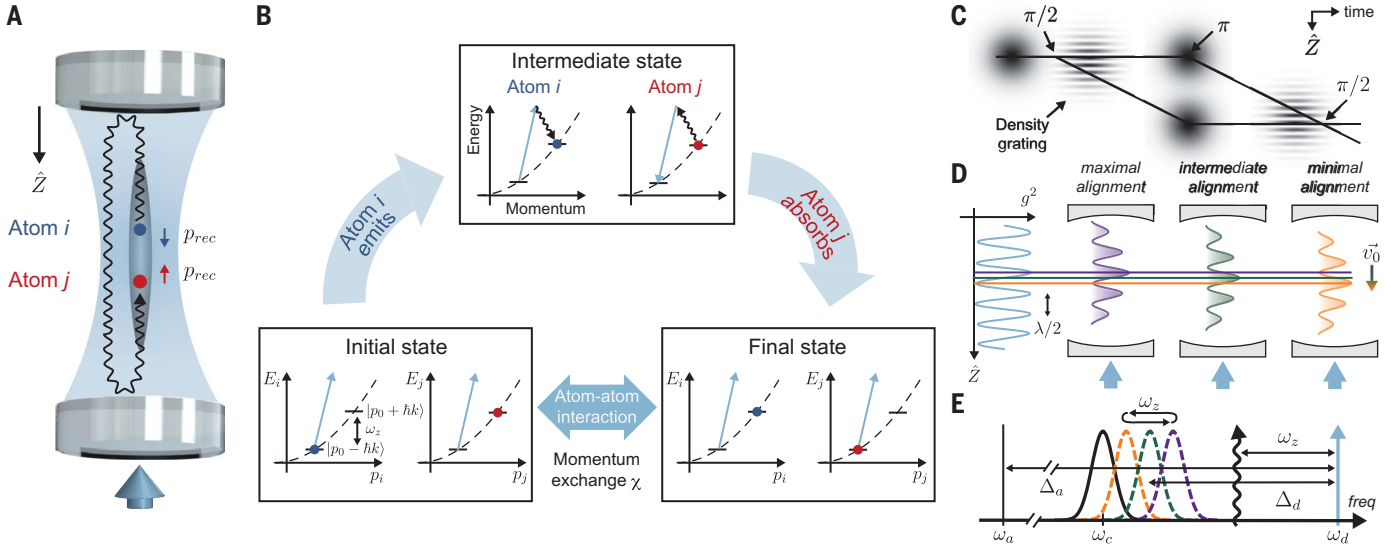

Fig. 1. Momentum exchange interaction. (**A**) A momentum-exchange interaction is realized between atoms in different momentum states ($p_0 \pm \hbar k)\hat{Z}$ by exchange of photons via a standing-wave optical cavity, illustrated for two particular atoms in red and blue. The dressing laser (light blue arrow) is injected into the cavity. (**B**) The energy versus momentum diagrams illustrate the steps of the momentum exchange between the example red and blue atoms. Adiabatic elimination of the virtual intermediate state leads to an effective momentum-exchange Hamiltonian involving only the atoms. (**C**) Space-time diagram of the matter-wave interferometer. Bragg pulses are applied to manipulate atoms in superpositions of momentum states, causing the wave packets to separate in time with subsequent pulses reoverlapping the wave packets. When the wave packets overlap with each other, their interference forms a density grating along $\hat{Z}$. (**D**) As the atomic density grating moves, its spatial overlap with the standing-wave cavity mode (light blue on the left) varies, with three snapshots in time (purple, green, and orange) shown on the right. (**E**) Frequency diagram of the optical atomic transition frequency ω_a (black solid line), bare cavity frequency ω_c with no atoms in the cavity (black solid Lorentzian), and the atom-dressed cavity resonance frequency (dashed purple, green, orange Lorentzians) for the corresponding snapshots in time from (D). The average dressing laser detuning Δ_d is shown. The cavity is frequency modulated at ω_z, leading to sidebands on the dressing laser at $\pm\omega_z$ (lower sideband shown as wiggly black line) that with the dressing laser couple the momentum states $p_0 \pm \hbar k$ to realize the momentum exchange.

F2 shown by the solid points and lines in Fig. 2A. This occurs when we tune a modulation sideband to be nominally on resonance with the dressed cavity by setting the dressing laser detuning from the average cavity resonance frequency (Fig. 1E) to $\Delta_d = \omega_z$. In this regime, the sideband light can escape from the cavity before being reabsorbed by the atoms, such that the collective population transfer can also be understood as a superradiant decay between momentum states (*18*, *20*, *21*). To confirm the collective nature of the decay, in a separate experiment, we prepare the initial superposition of states using an initial Bragg $\pi/2$-pulse 85 GHz detuned from the dressing laser. The difference in wave numbers of the dressing laser k_d and the Bragg laser k_{Bragg} causes a slip in the spatial alignment of the cavity standing wave and the atomic density grating by a phase $2|k_d - k_{Bragg}|L_{cloud} = 3.5$ radians across the axial extent $L_{cloud} = 1$ mm of the atomic cloud (Fig. 2B). In this case, we observe no superradiant transfer of population in Fig. 2A (open circles and dashed lines).

We now realize the momentum-exchange interaction by tuning the dressing laser so that the modulation sidebands are far from resonance with the cavity, i.e., $|\Delta_d \pm \omega_z| \gg \kappa/2$. In this limit, photons emitted at the sideband frequencies are more likely to be reabsorbed by the atoms than to escape from the cavity. This process of emitting and absorbing sideband photons leads to a momentum exchange as illustrated in Fig. 1, A and B.

Effective Hamiltonian

To model the momentum exchange process, we begin by defining $\hat{\psi}^\dagger(p)$ and $\hat{\psi}(p)$ as creation and annihilation field operators of an atom with momentum p that are related to creation and annihilation operators in position space by $\hat{\psi}(Z) = \int \hat{\psi}(p) e^{ipZ/\hbar} dp$. Because the wave packets centered at $p_0 \pm \hbar k$ have a narrow momentum spread $\hbar k \gg \sigma_p$, we define $\hat{\psi}_\uparrow(p) = \hat{\psi}(p + p_0 + \hbar k)$, $\hat{\psi}_\downarrow(p) = \hat{\psi}(p + p_0 - \hbar k)$ operators that annihilate atoms at momentum $p + p_0 \pm \hbar k$ within a momentum range $p \in [-\hbar k, +\hbar k]$. Doing this will support understanding in terms of both wave packets and an effective pseudospin language.

We divide the differential kinetic energy between the two momentum states $p + p_0 \pm \hbar k$ into two terms: a homogeneous or common kinetic energy difference $\hat{H}_z(p) = \frac{\hbar\omega_z}{2}\left[\hat{\psi}^\dagger_\uparrow(p)\hat{\psi}_\uparrow(p) - \hat{\psi}^\dagger_\downarrow(p)\hat{\psi}_\downarrow(p)\right]$ and an inhomogeneous contribution $\hat{H}_{in}(p) = \frac{\hbar\omega_{in}(p)}{2}\left[\hat{\psi}^\dagger_\uparrow(p)\hat{\psi}_\uparrow(p) - \hat{\psi}^\dagger_\downarrow(p)\hat{\psi}_\downarrow(p)\right]$ with $\omega_{in}(p) = 2kp/m$.

We can adiabatically eliminate the cavity fields using second-order perturbation theory (Fig. 1B), and in the perturbative limit $|\Delta_d \pm \omega_z| \gg \sqrt{N}\left|\frac{\alpha_d\sqrt{\kappa_1}}{\Delta_d + i\kappa/2}\right|\left|\frac{g_0^2}{4\Delta_a}\right|$, we obtain an effective atomic-only momentum-exchange Hamiltonian

$$\hat{H}_{mx} = \iint_{-\hbar k}^{\hbar k}\Big[\hbar\chi_+\hat{\psi}^\dagger_\uparrow(p)\hat{\psi}_\downarrow(p)\hat{\psi}^\dagger_\downarrow(q)\hat{\psi}_\uparrow(q) + \hbar\chi_-\hat{\psi}^\dagger_\downarrow(p)\hat{\psi}_\uparrow(p)\hat{\psi}^\dagger_\uparrow(q)\hat{\psi}_\downarrow(q)\Big]dp\,dq \quad (1)$$

with the total Hamiltonian $\hat{H} = \hat{H}_{mx} + \int_{-\hbar k}^{\hbar k}\hat{H}_{in}(p)dp + \int_{-\hbar k}^{\hbar k}\hat{H}_z(p)\,dp$. The momentum exchange couplings are given by

$$\chi_\pm = \left(\frac{g_0^2}{4\Delta_a}\right)^2 \frac{|\alpha_d|^2\kappa_1}{\Delta_d^2 + \kappa^2/4}\frac{\Delta_d \pm \omega_z}{(\Delta_d \pm \omega_z)^2 + \kappa^2/4} \quad (2)$$

where we have included finite cavity damping through appropriate Lindblad operators (*37*).To map this to a pseudospin model, we define ladder operators $\hat{j}_+(p) = \hat{\psi}^\dagger_\uparrow(p)\hat{\psi}_\downarrow(p)$, $\hat{j}_-(p) = \hat{\psi}^\dagger_\downarrow(p)\hat{\psi}_\uparrow(p)$ and spin projection operators $\hat{j}_x(p) = \frac{1}{2}\left[\hat{j}_+(p) + \hat{j}_-(p)\right]$, $\hat{j}_y(p) = \frac{1}{2i}\left[\hat{j}_+(p) - \hat{j}_-(p)\right]$, and $\hat{j}_z(p) = \frac{1}{2}\left[\hat{\psi}^\dagger_\uparrow(p)\hat{\psi}_\uparrow(p) - \hat{\psi}^\dagger_\downarrow(p)\hat{\psi}_\downarrow(p)\right]$. Integrating over all momentum states, we can then define collective operators $\hat{J}_\alpha = \int_{-\hbar k}^{\hbar k}\hat{j}_\alpha(p)\,dp$, where $\alpha \in [x, y, z, +, -]$. The momentum-exchange Hamiltonian $\hat{H}_{mx}$ is then equivalent to an effective spin-exchange Hamiltonian $\hat{H}_{sx} = \chi_+\hat{J}_+\hat{J}_- + \chi_-\hat{J}_-\hat{J}_+$. This can be viewed as a

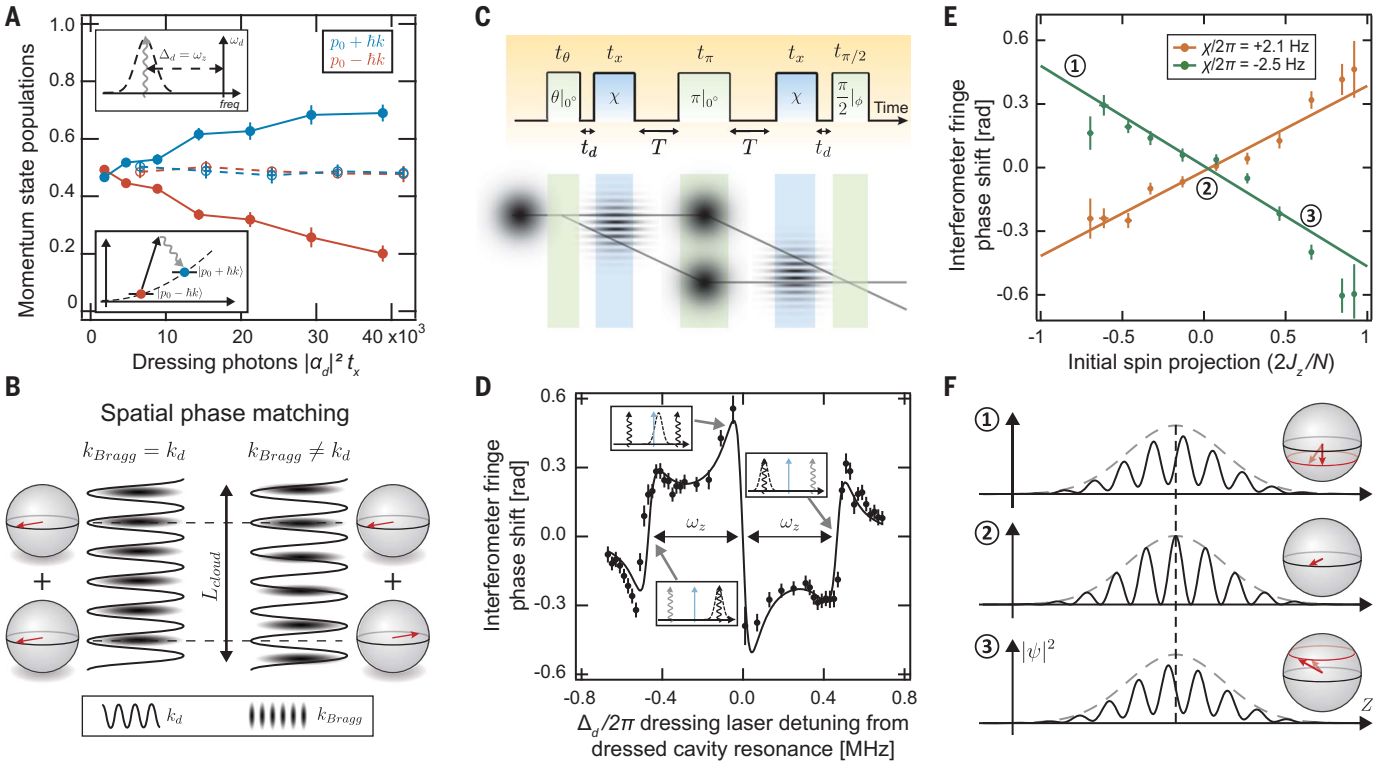

Fig. 2. Modulation sidebands and one-axis twisting dynamics. (**A**) When a modulation sideband generated by the moving atomic density grating is tuned to resonance with the cavity (top inset), the light escapes the cavity and population is collectively or superradiantly transferred (bottom inset) between the two momentum states at $p_0 \pm \hbar k$ (solid points and lines). After breaking the phase-matching condition, we observe no superradiant transfer of population (open circles and dashed lines). (**B**) The system is well phase matched when the wave numbers of the Bragg laser (that generates the density grating) and the dressing laser (that drives the momentum-exchange interaction) closely match each other (on the left). A difference in wave number ($k_{\mathrm{Bragg}} \neq k_{\mathrm{d}}$) will lead to a spatially varying phase that eliminates the superradiance (on the right). (**C**) Matter-wave interferometer sequence and space-time diagram for observing all-to-all Ising or one-axis twisting dynamics. The interferometer fringe amplitude and phase shift $\Delta\phi$ are measured by scanning the phase of the final rotation φ. (**D**) The observed phase shift $\Delta\phi$ of the interferometer fringe versus the dressing laser's detuning from the dressed cavity resonance, displaying the predicted (line) functional form of χ from Eq. 2. The insets illustrate the relative alignment of the modulation sideband to the cavity resonance for three characteristic detunings. (**E**) The measured interferometer phase shift scales linearly with the initial spin projection $J_z = \langle \hat{J}_z \rangle$, while holding Δ_{d} fixed. The orange data points and fitted line are for $\chi/2\pi = +2.1$ Hz, and the green data points and fitted line are for $\chi/2\pi = -2.5$ Hz). (**F**) Visualizations of the phase shift $\Delta\phi$ in both the pseudospin picture (Bloch spheres) and in the atomic density grating picture for three characteristic points in (E).

collective XX-Heisenberg or Richardson-Gaudin integrable model where the nonlocal spin-spin couplings χ compete with an inhomogeneous axial field—a model often used in quantum magnetism and superconductivity through the spin Anderson mapping (*30*–*32*). The standing-wave cavity mode's spatial intensity variation $\cos^2 kZ$ produces additional terms $\hat{J}_+^2$ and $\hat{J}_-^2$ that we can neglect because these terms are not resonant or equivalently do not conserve energy (*37*, *39*).

One-axis twisting dynamics

The exchange Hamiltonian can be rewritten as $\hat{H}_{\mathrm{sx}} \approx \chi\left(\hat{J}^2 - \hat{J}_z^2\right)$ with $\chi = \chi_+ + \chi_-$, ignoring single-particle terms. At the mean-field level, the one-axis twisting Hamiltonian $\chi \hat{J}_z^2 \approx 2\chi\langle \hat{J}_z \rangle \hat{J}_z$ induces a rotation of the collective Bloch vector about the z direction at a constant frequency, $2\chi\langle \hat{J}_z \rangle$, that depends on the initial momentum population difference $\langle \hat{J}_z \rangle$, which is conserved by the Hamiltonian $\hat{H}_{\mathrm{sx}}$. In the equivalent matter-wave picture, the azimuthal phase, $\Delta\phi = 2\chi\langle \hat{J}_z \rangle t_x$, accumulated when the exchange interaction is applied for a time t_x, appears as a shift of the spatial interference fringe between the two wave packets (Fig. 2F).

To observe this phase shift, we run a matter-wave interferometer sequence (Fig. 2C) beginning with a Bragg $\pi/4$-pulse lasting 15 μs that prepares the atoms with population difference $\frac{\langle \hat{J}_z \rangle}{N/2} \approx -0.7$. After waiting a delay time $t_{\mathrm{d}} = 25\,\mu\mathrm{s}$, we apply the dressing laser to create the exchange interaction for $t_x = 25$ μs. To reoverlap the wave packets or equivalently undo the inhomogeneity from $\hat{H}_{\mathrm{in}}$, we then apply a Bragg π-pulse and apply the dressing laser again before applying a final Bragg $\pi/2$-pulse with varying phase ϕ. The final $\pi/2$-pulse maps the phase shift $\Delta\phi$ into a change in $\langle \hat{J}_z \rangle$. We measure the population in each momentum state by using velocity-sensitive Raman π-pulses and cavity-assisted quantum nondemolition measurements (*12*, *37*). We repeat the experiment while scanning the phase of the final $\pi/2$-pulse. The phase shift $\Delta\phi$ is then determined from the phase of the observed fringe $\langle \hat{J}_z \rangle$ versus ϕ.

The momentum-exchange coupling of Eq. 2 predicts a triple-dispersive structure as the detuning of the dressing laser Δ_{d} varies. We observe this predicted structure in Fig. 2D by measuring the induced phase shift $\Delta\phi$ as we vary the dressing laser detuning Δ_{d} from the dressed cavity resonance. In these data, the incident dressing laser power (350 photons/μs) is held fixed. The two outer dispersive features arise as the two sideband frequencies at $\pm\omega_z$ pass through resonance with the cavity as shown in the corresponding insets. The dispersive feature near $\Delta_{\mathrm{d}} = 0$ arises from the

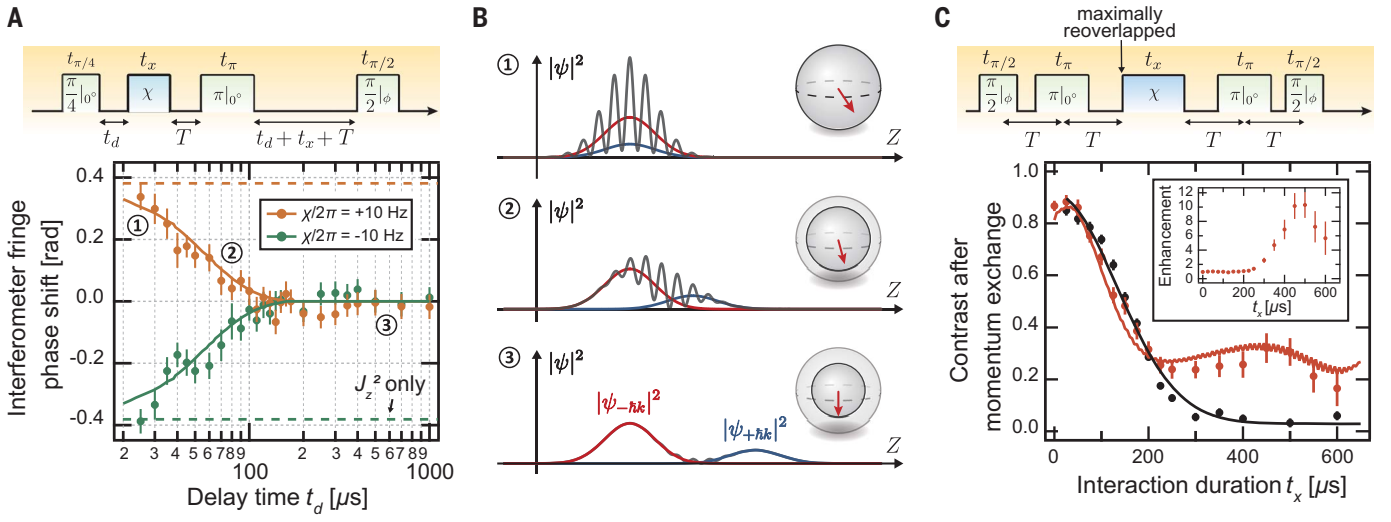

Fig. 3. Decoherence and energy gap protection. (**A**) The measured OAT phase shift goes to zero if the momentum-exchange interaction is applied after a delay time t_d (see pulse sequence in top panel). After the atomic wave packets separate for various delay times, the measured OAT phase shift for both positive and negative χ are shown in solid points with the simulations in solid lines. For comparison, the dashed lines are the simulated result with a pure OAT $\hat{J}_z^2$ Hamiltonian instead of the full momentum-exchange Hamiltonian. (**B**) Illustration of the wave packet separation and pseudospin representation at characteristic points in (A). As the wave packets separate, the atomic density grating disappears and the modulation sidebands that create the momentum-exchange interaction are no longer generated. Corresponding pseudospin Bloch spheres are shown. (**C**) Using the sequence in the top panel, the bottom panel shows the contrasts of the interferometer fringe measured at the end of the exchange interaction period with $\chi = 0$ (black symbols), $\chi/2\pi = 6$ Hz (red symbols). The ratio between the two (inset) displays significant gap protection of coherence owing to the momentum-exchange's $\hat{J}^2$ contribution. The simulated results (solid lines) show good agreement with the data.

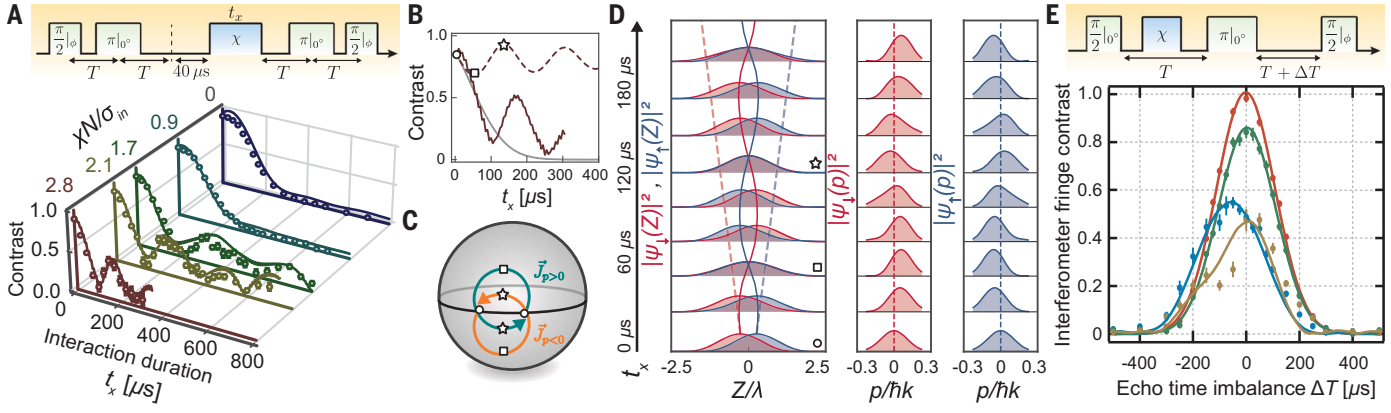

Fig. 4. Binding wave packets together. (**A**) We run a sequence similar to that of Fig. 3C except with an additional 40-μs delay after wave packet overlap before application of the dressing laser for a variable time t_x. We see that as the interaction strength is increased relative to the RMS inhomogeneous broadening $\sigma_{in} = 2\pi \times 2$ kHz, there is a transition in the dynamics for $N\chi/\sigma_{in} > 0.9$. Notably, there are also clear oscillations that were only hinted at in Fig. 3C. The lines are theory predictions. (**B**) The theory predictions with residual superradiance on (solid) and turned off (dashed) are shown with three example points in the oscillations labeled; the prediction with no interactions is shown in gray. (**C**) The total length of the pseudospin Bloch vector $\vec{J}$ oscillates in time because the individual Bloch vectors oscillate as shown for $\vec{J}_{p>0}$ and $\vec{J}_{p<0}$ in green and orange, respectively, with $\chi N/\sigma_{in} = 2.8$. (**D**) (Left) In a co-moving frame, the wave packets oscillate in time about their average position in space (blue and red wave packets and centers, solid lines; noninteracting system, dashed lines). The momentum-space wave packets (right) also oscillate but with a $\pi/2$ phase shift in time relative to the position space wave packets, as would be the case for a harmonic oscillator. (**E**) The interferometer contrast as a function of imbalance in the time from nominal perfect reoverlap of the wave packets with no momentum-exchange (red data and fit), momentum-exchange applied right after first $\pi/2$ at intermediate power (blue data and theory) and high power (brown data and theory), and momentum-exchange applied when wave packets are separated (green data and fit).

carrier passing through resonance with the cavity. At $\Delta_d = 0$, the exchange interaction parameters are $\chi_+ \approx -\chi_-$, leading to a cancellation of the total exchange interaction ($\chi \approx 0$).

The phase shift $\Delta\phi$ is expected to scale linearly with $\langle \hat{J}_z \rangle$. We observe this by replacing the initial $\pi/4$-pulse with variable-length pulses to vary $\langle \hat{J}_z \rangle$ while holding Δ_d fixed instead. For the orange data in Fig. 2E, the frequency of the relevant sideband is higher than the cavity resonance frequency, leading to a measured $\chi/2\pi = +2.1$ Hz. For the green data, we retune

the detuning Δ_d so that the relevant sideband frequency is lower than the cavity resonance frequency, leading to a measured $\chi/2\pi = -2.5$ Hz. We observe a linear phase shift $\Delta\phi$ for $\chi > 0$ and $\chi < 0$ with opposite slopes, as expected.

We observe that the size of the phase shift F4 $\Delta\phi$ decreases if the wave packets are allowed to separate for a time t_d before applying the dressing laser for time $t_x = 25\,\mu s$ to induce F3 the momentum-exchange interaction. Figure 3A (top) shows the pulse sequence used to measure this decay of the phase shift (bottom) for both positive and negative χ (orange and green points). For comparison, the solid lines indicate the predicted phase shifts for the full momentum-exchange Hamiltonian, whereas the dashed lines indicate the predicted phase shift for an OAT Hamiltonian $-\chi\hat{J}_z^2$. The wave packet separation or equivalently the inhomogeneity $\hat{H}_{in}$ would not affect a pure OAT Hamiltonian as was the case in (*12*), whereas the phase shift is decreased by dephasing for exchange interaction as was observed in a spin system (*3*). The wave packet separation leads to dephasing or shortening of the Bloch vector as visualized in Fig. 3B. As the wave packets separate, the corresponding collective Bloch vectors are shortened while the projection $\langle \hat{J}_z \rangle$ is conserved.

Gap protection: Binding wave packets together

The additional nonlinear term $\hat{J}^2$ in the momentum-exchange Hamiltonian gives rise to a many-body energy gap between states of higher symmetry (large J) and lower symmetry (smaller J) (*3*, *27*). To explore how matter-wave coherence is protected by the gap, we run a Mach-Zehnder interferometer as shown in Fig. 3C (top), in which we apply the dressing laser for a time t_x starting at the point of maximum reoverlap of the wave packets (with $T = 70\,\mu s$). The coherence at the end of the dressing laser application is estimated from the amplitude of the interferometer fringe by using an appropriately timed π-pulse and a final $\pi/2$-pulse shown. To account for the atomic loss resulting from free-space scattering and superradiance into higher-momentum states, the contrast is calculated by normalizing the fitted fringe amplitude to the residual population in the two momentum states $p_0 \pm \hbar k$. The actual coherence of the system is higher owing to the finite possibility of underestimating the number of atoms that underwent free-space scattering. In Fig. 3C, the experiment is performed with the dressing laser off ($\chi = 0$, black points and fitted black curve) and the dressing laser on ($\chi/2\pi = 6$ Hz, red points and red theory curve); for the latter, we observe that appreciable fringe contrast extends out to 600 μs. The inset of Fig. 3C shows that the momentum-exchange enhances the contrast by as much as a factor of 10(2).

In Fig. 3C, the coherence undergoes a slight rise before ultimately falling. This behavior can be accentuated by allowing the wave packets to undergo a small amount of separation for 40 μs before applying the momentum-exchange interactions for a duration t_x. With $T = 70\,\mu s$, the observed interferometer contrast versus t_x (Fig. 4A) is measured at different dressing laser powers to obtain different ratios of χN to the RMS inhomogeneity from $\hat{H}_{in}$ expressed as a frequency σ_{in}. We observe a sharp transition in the dynamical behavior between $\chi N/\sigma_{in} = 0.9$ and 1.7 with the emergence of oscillations of the contrast that extend to long times as χN increases. The oscillations become faster and have larger amplitudes at shorter times as χN increases. This behavior is reasonably consistent with the overlayed theory simulations (colored traces in Fig. 4A) that include finite superradiance and where only σ_{in} is fit from the data with $\chi N = 0$.

The extension of coherence to longer times and the observed oscillations can be understood as the momentum-exchange interaction causing the wave packets to become bound to each other such that they no longer freely separate. In Fig. 4B, we show the simulated variation of the contrast versus time without superradiance, highlighting three example points that we explain using the simulated trajectories in Fig. 4C for the collective pseudospin Bloch vectors evaluated for $p > 0$ or $p < 0$ with $\vec{J}_{p\geq 0} = \int_0^{\hbar k} \vec{j}(p)dp$ and $\vec{J}_{p<0} = \int_{-\hbar k}^{0} \vec{j}(p)dp$ where $\vec{j}(p) = \hat{j}_x(p)\hat{x} + \hat{j}_y(p)\hat{y} + \hat{j}_z(p)\hat{z}$. In Fig. 4D, we also show the simulated results without superradiance for the individual wave packets in both momentum and position space. In the pseudospin picture, the momentum-exchange causes the displayed vectors $\vec{J}_{p>0}$ and $\vec{J}_{p<0}$ to undergo orbits that oscillate symmetrically above and below the equator such that the total Bloch vector length oscillates in time. In the wave packet picture, with no interactions, the wave packet centers would follow the diverging dashed lines. With interactions, the wave packets oscillate in position with respect to each other, while also oscillating in their momentum p, as though the wave packets are now connected by a spring with characteristic frequency set by the exchange interaction strength χN in the limit that $\chi N \gg \sigma_{in}$ and for small wave packet separation. If the wave packets are allowed to initially separate before the spring-like coupling is turned on, then the amplitude of the oscillations of the wave packet separations (and hence the contrast) will be larger, as was observed in Fig. 4A.

To further explore this idea of wave packets becoming bound to each other, we run a Mach-Zehnder matter-wave interferometer with the echo times imbalanced by ΔT as shown in Fig. 4E (top), with fixed T=1.05 ms. If the exchange interaction is not applied (Fig. 4E, red points and fit), then the fringe contrast is maximized when the echo time imbalance is $\Delta T = 0$ because this is when the wave packets have maximal reoverlap. If the momentum exchange interaction is applied just after the first splitting pulse, we see that the point of maximum contrast is shifted to $\Delta T = -55\,\mu s$ (blue points and simulation), and becomes non-Gaussian (brown points and simulation) at even higher dressing laser power. We rule out single-particle effects that might also shift the maximal reoverlap time by repeating the experiment, but with the dressing laser applied 1 ms after the first splitting pulse when the wave packets are not overlapped (green points and fit), which also suppresses collective superradiance, leading to the higher observed contrast. The fact that the delay is modified by 55 μs rather than $t_x = 25\,\mu s$ (as one might naïvely expect should one think of the wave packet separation as being frozen in place during the exchange interaction) arises from a 25-μs delay between the end of the $\pi/2$-pulse and the beginning of the interaction, as well as the harmonic-oscillator–like nature of the coupling of the wave packets.

To emphasize how unusual it is that the wave packets bind to each other, consider a gedankenexperiment in which a single photon combined with a coherent state of light drives the two-photon Bragg transition with total momentum transfer to the atomic cloud $2\hbar k$. Given that one cannot tell which atom underwent the two-photon transition, the initial state should be symmetrized with respect to which atom absorbed the single photon, analogous to a Dicke or W state (*37*). Without exchange interactions, at long times one would observe a single atom eventually emerge from the cloud with velocity $v_{rec} = (2\hbar k)/m$ while all other atoms remain at their initial momentum. By contrast, with the momentum-exchange interaction, one would never observe a single atom emerge with velocity v_{rec}. Instead, the whole cloud of N atoms would collectively recoil with velocity v_{rec}/N (*37*).

This collective recoil is analogous to Mössbauer spectroscopy (or Lamb-Dicke spectroscopy) in which atoms embedded in a crystal cause the whole crystal to recoil when the atoms absorb light. In our case, the collective recoil mechanism, enabled by strong exchange interactions, suppresses Doppler dephasing or line broadening. However, unlike in Mössbauer spectroscopy, the collective nature of the recoil does not suppress the photon recoil shift, which here defines the transition frequency ω_z between the two momentum states.

Discussion and outlook

The collective recoil mechanism observed here allows for the sensing of accelerations a_Z such as that caused by gravity (*37*), given that the phase difference that accrues between the two momentum states depends on ω_z, which chirps as $\omega_z \rightarrow 2k(p_0/m + a_Z t)$. Equivalently,

the atoms act as a phase memory of the optical Bragg pulses with which they interact (*40*). This opens interesting paths for enhancing quantum memory lifetime (*41*), for Doppler-broadening–free spectroscopy, and for matter-wave interferometers that do not rely on spin-echo–like sequences and therefore would also allow measurements of velocities rather than accelerations.

Finally, the momentum-exchange Hamiltonian that we demonstrated here is equivalent to the model Hamiltonian often used to describe Bardeen–Cooper–Schrieffer (BCS) s-wave superconductors. From this perspective, the observed oscillations can be identified with Higgs oscillations following a quench of the exchange interaction strength (*30*, *42*–*44*). This would enable quantum simulation of BCS superfluidity and also sets the stage for quantum simulation that goes beyond two-level systems by encoding degrees of freedom in the larger ladder of momentum states (*45*, *46*) as well as internal states (*47*–*52*). The large number of synthetic dimensions, in combination with the long-range cavity-mediated interactions, open new opportunities for the emulation of self-generated spin-orbit coupling (*53*, *54*), pair production (*2*, *55*–*61*), topological superfluidity (*62*), and dynamical gauge fields (*63*–*67*). Lastly, the generation of sideband tones may open a path to transduce excitations between matter waves and mesoscopic opto-mechanical systems (*25*, *26*) or back-action–evading measurements of matter waves as proposed for spins (*68*).

REFERENCES AND NOTES

1. I. D. Leroux, M. H. Schleier-Smith, V. Vuletić, *Phys. Rev. Lett.* **104**, 073602 (2010).
2. E. J. Davis, G. Bentsen, L. Homeier, T. Li, M. H. Schleier-Smith, *Phys. Rev. Lett.* **122**, 010405 (2019).
3. M. A. Norcia *et al*., *Science* **361**, 259–262 (2018).
4. J. A. Muniz *et al*., *Nature* **580**, 602–607 (2020).
5. N. Sauerwein *et al*., *Nat. Phys.* **19**, 1128–1134 (2023).
6. A. T. Black, H. W. Chan, V. Vuletić, *Phys. Rev. Lett.* **91**, 203001 (2003).
7. K. Baumann, C. Guerlin, F. Brennecke, T. Esslinger, *Nature* **464**, 1301–1306 (2010).
8. S. C. Schuster, P. Wolf, S. Ostermann, S. Slama, C. Zimmermann, *Phys. Rev. Lett.* **124**, 143602 (2020).
9. Y. Guo *et al*., *Nature* **599**, 211–215 (2021).
10. P. Kongkhambut *et al*., *Science* **377**, 670–673 (2022).
11. R. M. Kroeze, Y. Guo, V. D. Vaidya, J. Keeling, B. L. Lev, *Phys. Rev. Lett.* **121**, 163601 (2018).
12. G. P. Greve, C. Luo, B. Wu, J. K. Thompson, *Nature* **610**, 472–477 (2022).
13. K. C. Cox, G. P. Greve, J. M. Weiner, J. K. Thompson, *Phys. Rev. Lett.* **116**, 093602 (2016).
14. O. Hosten, N. J. Engelsen, R. Krishnakumar, M. A. Kasevich, *Nature* **529**, 505–508 (2016).
15. E. Pedrozo-Peñafiel *et al*., *Nature* **588**, 414–418 (2020).
16. J. M. Robinson *et al*., *Nat. Phys.* **20**, 208–213 (2024).
17. I. D. Leroux, M. H. Schleier-Smith, V. Vuletić, *Phys. Rev. Lett.* **104**, 250801 (2010).
18. D. Kruse, C. von Cube, C. Zimmermann, P. W. Courteille, *Phys. Rev. Lett.* **91**, 183601 (2003).
19. F. Brennecke, S. Ritter, T. Donner, T. Esslinger, *Science* **322**, 235–238 (2008).
20. M. Wolke, J. Klinner, H. Keßler, A. Hemmerich, *Science* **337**, 75–78 (2012).
21. H. Keßler, J. Klinder, M. Wolke, A. Hemmerich, *New J. Phys.* **16**, 053008 (2014).
22. P. Münstermann, T. Fischer, P. Maunz, P. W. H. Pinkse, G. Rempe, *Phys. Rev. Lett.* **84**, 4068–4071 (2000).
23. R. Mottl *et al*., *Science* **336**, 1570–1573 (2012).
24. N. Spethmann, J. Kohler, S. Schreppler, L. Buchmann, D. M. Stamper-Kurn, *Nat. Phys.* **12**, 27–31 (2016).
25. R. A. Thomas *et al*., *Nat. Phys.* **17**, 228–233 (2021).
26. R. D. Delaney *et al*., *Nature* **606**, 489–493 (2022).
27. E. J. Davis *et al*., *Phys. Rev. Lett.* **125**, 060402 (2020).
28. A. Shankar, L. Salvi, M. L. Chiofalo, N. Poli, M. J. Holland, *Quantum Sci. Technol.* **4**, 045010 (2019).
29. J. D. Wilson *et al*., *Phys. Rev. A* **106**, 043711 (2022).
30. J. Marino, M. Eckstein, M. S. Foster, A. M. Rey, *Rep. Prog. Phys.* **85**, 116001 (2022).
31. R. Richardson, N. Sherman, *Nucl. Phys.* **52**, 221–238 (1964).
32. R. Richardson, N. Sherman, *Nucl. Phys.* **52**, 253–268 (1964).
33. F. Finger *et al*., *Phys. Rev. Lett.* **132**, 093402 (2024).
34. R. V. Pound, G. A. Rebka Jr., *Phys. Rev. Lett.* **4**, 337–341 (1960).
35. T. Bothwell *et al*., *Nature* **602**, 420–424 (2022).
36. K. C. Cox, G. P. Greve, B. Wu, J. K. Thompson, *Phys. Rev. A* **94**, 061601 (2016).
37. See the supplementary materials.
38. Z. Chen, J. G. Bohnet, J. M. Weiner, K. C. Cox, J. K. Thompson, *Phys. Rev. A* **89**, 043837 (2014).
39. J. Borregaard, E. Davis, G. S. Bentsen, M. H. Schleier-Smith, A. S. Sørensen, *New J. Phys.* **19**, 093021 (2017).
40. M. A. Norcia, J. R. K. Cline, J. K. Thompson, *Phys. Rev. A* **96**, 042118 (2017).
41. A. T. Black, J. K. Thompson, V. Vuletić, *Phys. Rev. Lett.* **95**, 133601 (2005).
42. R. J. Lewis-Swan *et al*., *Phys. Rev. Lett.* **126**, 173601 (2021).
43. D. J. Young *et al*., *Nature* **625**, 679–684 (2024).
44. S. Smale *et al*., *Sci. Adv.* **5**, eaax1568 (2019).
45. F. A. An, E. J. Meier, J. Ang'ong'a, B. Gadway, *Phys. Rev. Lett.* **120**, 040407 (2018).
46. E. J. Meier *et al*., *Science* **362**, 929–933 (2018).
47. A. Celi *et al*., *Phys. Rev. Lett.* **112**, 043001 (2014).
48. T. Chalopin *et al*., *Nat. Phys.* **16**, 1017–1021 (2020).
49. B. K. Stuhl, H. I. Lu, L. M. Aycock, D. Genkina, I. B. Spielman, *Science* **349**, 1514–1518 (2015).
50. S. Kolkowitz *et al*., *Nature* **542**, 66–70 (2017).
51. M. Mancini *et al*., *Science* **349**, 1510–1513 (2015).
52. F. Mivehvar, H. Ritsch, F. Piazza, *Phys. Rev. Lett.* **122**, 113603 (2019).
53. F. Mivehvar, F. Piazza, T. Donner, H. Ritsch, *Adv. Phys.* **70**, 1–153 (2021).
54. T. Chanda, R. Kraus, G. Morigi, J. Zakrzewski, *Quantum (Vienna)* **5**, 501 (2021).
55. R. Ma *et al*., *Phys. Rev. Lett.* **107**, 095301 (2011).
56. F. Meinert, *Phys. Rev. Lett.* **116**, 205301 (2016).
57. W. Xu, W. Morong, H.-Y. Hui, V. W. Scarola, B. DeMarco, *Phys. Rev. A* **98**, 023623 (2018).
58. B. Lücke *et al*., *Science* **334**, 773–776 (2011).
59. C. Gross, *J. Phys. At. Mol. Opt. Phys.* **45**, 103001 (2012).
60. S. J. Masson, M. D. Barrett, S. Parkins, *Phys. Rev. Lett.* **119**, 213601 (2017).
61. A. Periwal *et al*., *Nature* **600**, 630–635 (2021).
62. C. V. Kraus, M. Dalmonte, M. A. Baranov, A. M. Läuchli, P. Zoller, *Phys. Rev. Lett.* **111**, 173004 (2013).
63. W. Zheng, N. R. Cooper, *Phys. Rev. Lett.* **117**, 175302 (2016).
64. C. Schweizer *et al*., *Nat. Phys.* **15**, 1168–1173 (2019).
65. E. Colella, A. Kosior, F. Mivehvar, H. Ritsch, *Phys. Rev. Lett.* **128**, 070603 (2022).
66. R. Rosa-Medina *et al*., *Phys. Rev. Lett.* **128**, 143602 (2022).
67. H. Zhang, A. Chu, C. Luo, J. K. Thompson, A. M. Rey, *Phys. Rev. Res.* **5**, L032039 (2023).
68. A. Shankar, G. P. Greve, B. Wu, J. K. Thompson, M. Holland, *Phys. Rev. Lett.* **122**, 233602 (2019).
69. C. Luo, Raw Data for Cavity-Mediated Collective Momentum-Exchange Interactions, dataset, CU Scholar (2023); https://doi.org/10.25810/6AH7-DR67.

ACKNOWLEDGMENTS

We acknowledge helpful discussions with E. Polzik, M. Schleier-Smith, and A. Shankar. **Funding:** This material is based upon work supported by the US Department of Energy, Office of Science, National Quantum Information Science Research Centers, Quantum Systems Accelerator. We acknowledge additional funding support from the National Science Foundation under grant nos. 2317149 (Physics Frontier Center) and OMA-2016244 (QLCI), NIST, and DARPA/ARO W911NF-19-1-0210 and W911NF-16-1-0576, AFOSR grants FA9550-18-1-0319 and FA9550-19-1-0275, and Vannevar Bush Faculty Fellowship. **Author contributions:** C.L. and V.P.W.K. contributed to the building of the experiment, the data taking, and the data analysis. J.K.T. conceived and supervised the experiments. H.Z., J.D.W., and A.C. contributed to the theoretical derivation and numerical simulations supervised by M.J.H. and A.M.R. C.L., H.Z., and J.K.T. wrote the manuscript with feedback from A.M.R. All authors discussed the experimental implementation and the results, and contributed to the manuscript. **Competing interests:** The authors declare no competing interests. **Data and materials availability:** The datasets generated during and/or analyzed during this study are available in the CU Scholar repository (*69*).

SUPPLEMENTARY MATERIALS

science.org/doi/10.1126/science.adi1393
Materials and Methods
Supplementary Text
Figs. S1 to S5
Reference (*70*)

Submitted 17 April 2023; accepted 21 March 2024
10.1126/science.adi1393